Don't Blink: Constraining the Circumstellar Environment of the Interacting Type Ia Supernova 2015cp

C. E. Harris[1,2], P. E. Nugent[1,2], A. Horesh[3], J. S. Bright[4], R. P. Fender[4], M. L. Graham[1,5], K. Maguire[6], M. Smith[7], N. Butler[8], S. Valenti[9], A. V. Filippenko[1,10], O. Fox[11], A. Goobar[12], P. L. Kelly[1,13], and K. J. Shen[1]

[1] Department of Astronomy, University of California, Berkeley, CA 94720-3411, USA; chelseaharris@lbl.gov
[2] Lawrence Berkeley National Laboratory, 1 Cyclotron Road, MS 50B-4206, Berkeley, CA 94720, USA
[3] Racah Institute of Physics, The Hebrew University of Jerusalem, Jerusalem, 91904, Israel
[4] Astrophysics, Department of Physics, University of Oxford, Denys Wilkinson Building, Keble Road, Oxford OX1 3RH, UK
[5] Department of Astronomy, University of Washington, Box 351580, U.W., Seattle, WA 98195-1580, USA
[6] Astrophysics Research Centre, School of Mathematics and Physics, Queens University Belfast, Belfast BT7 1NN, UK
[7] Department of Physics and Astronomy, University of Southampton, Southampton SO17 1BJ, UK
[8] School of Earth and Space Exploration, Arizona State University, Tempe, AZ 85287, USA
[9] Department of Physics, University of California, Davis, 1 Shields Avenue, Davis, CA 95616, USA
[10] Miller Senior Fellow, Miller Institute for Basic Research in Science, University of California, Berkeley, CA 94720, USA
[11] Space Telescope Science Institute, 3700 San Martin Drive, Baltimore, MD 21218, USA
[12] The Oskar Klein Centre, Department of Physics, Stockholm University, AlbaNova, SE-106 91 Stockholm, Sweden
[13] School of Physics & Astronomy, University of Minnesota, 116 Church Street S.E., Minneapolis, MN 55455, USA

Abstract

Despite their cosmological utility, the progenitors of Type Ia supernovae (SNe Ia) are still unknown, with many efforts focused on whether accretion from a nondegenerate companion can grow a carbon–oxygen white dwarf to near the Chandrasekhar mass. The association of SNe Ia resembling SN 1991T ("91T-like") with circumstellar interaction may be evidence for this "single-degenerate" channel. However, the observed circumstellar medium (CSM) in these interacting systems is unlike a stellar wind—of particular interest, it is sometimes detached from the stellar surface, residing at $\sim 10^{16}$ cm. A *Hubble Space Telescope (HST)* program to discover detached CSM around 91T-like SNe Ia successfully discovered interaction nearly two years after explosion in SN 2015cp (Graham et al. 2018). In this work, we present radio and X-ray follow-up observations of SN 2015cp and analyze them in the framework of Harris et al. (2016) to limit the properties of a constant-density CSM shell in this system. Assuming the *HST* detection took place shortly after the shock crossed the CSM, we constrain the total CSM mass in this system to be $<0.5\,M_{\odot}$. This limit is comparable to the CSM mass of supernova PTF11kx, but does not rule out lower masses predicted for recurrent novae. From lessons learned modeling PTF11kx and SN 2015cp, we suggest a strategy for future observations of these events to increase the sample of known interacting SNe Ia.

Key words: binaries: symbiotic – supernovae: general – supernovae: individual (SN 2015cp) – stars: mass-loss

1. Introduction

Broadly speaking, Type Ia supernovae (SNe Ia) are hydrogen-deficient thermonuclear explosions of white dwarfs (see, e.g., Filippenko 1997, for a review of SNe and their optical spectra). The landscape of the debate regarding the detailed nature of Type Ia supernova (SN Ia) progenitors has not changed much since the 1980s, despite the use of SNe Ia as increasingly precise cosmological tools. The review by Branch et al. (1995), which concludes that "the coalescence of pairs of [carbon–oxygen] white dwarfs, and the accretion of hydrogen on a thermal timescale via Roche-lobe overflow from subgiant donors, are the two most promising candidate progenitor mechanisms for SNe Ia," and "there is no strong objection to the notion that several, or even all, candidates contribute," still largely holds today. The first scenario involving two carbon–oxygen white dwarfs (CO WDs) is typically referred to as the "double-degenerate" (DD) channel, and the second, which involves a nondegenerate companion, is the "single-degenerate" (SD) channel. Two significant changes since this review are that the helium-shell detonation ("double-detonation") variant of the DD channel has been brought back into the mainstream (e.g., Fink et al. 2010; Shen & Moore 2014), and some authors suggest a variant of the DD scenario in which the CO WD merges with the degenerate core of an asymptotic giant branch (AGB) companion (e.g., Soker 2013).

Generally, though, efforts have been focused on distinguishing whether SD or DD is the dominant channel for forming SNe Ia. One of the identifying characteristics of the SD channel is that it can create a dense, extended, hydrogen-rich circumstellar medium (CSM), while DD companions do not—hydrogen-rich material from DD channels is swept over within a few days, or is quite distant ($\gtrsim 10^{17}$ cm) and low density (e.g., Raskin & Kasen 2013; Shen et al. 2013). From deep radio limits searching for SN ejecta interaction with a red-giant (RG) wind, Chomiuk et al. (2016) constrain the occurrence of RG companions for normal SNe Ia to $<10\%$. Yet there is evidence that some SNe Ia have circumstellar gas: a small number of SNe Ia, called "Type Ia-CSM" by Silverman et al. (2013a) who characterized the population, are observed to interact with extremely dense CSM. As noted by Silverman et al. (2013a) and Leloudas et al. (2015), all are spectroscopically like SN 1991T (Filippenko et al. 1992) or SN 1999aa (Garavini et al. 2004), i.e., they have strong Fe III and weak Si II lines near-maximum light (Branch et al. 1993). Hereafter, we will use the term "91T-like" to mean resembling either of these SNe, rather than requiring the very weak Ca II H and K absorption characteristic of SN 1991T itself. The association of interaction with only this subgroup,

which is also associated with younger stellar populations, raises the question of whether 91T-like SNe Ia have different progenitors compared to normal SNe Ia—they may represent an SD channel for forming SNe Ia.

Though not distinguished by Silverman et al. (2013a), interacting SNe actually fall into two categories: those with prompt interaction, and those with delayed interaction. In the SN Ia-CSM class, the two instances of the latter scenario are SN 2002ic (Wood-Vasey et al. 2004) and PTF11kx (Dilday et al. 2012). The transition of PTF11kx from normal to interacting was well observed both spectroscopically and photometrically. Such transitions have also been reported in a few SNe Ib (Milisavljevic et al. 2015; Mauerhan et al. 2018), and SN 1987A provides a famous, though extreme, example from the Type II class (Larsson et al. 2011; Fransson et al. 2015). To encompass the delayed interaction group, we use the label Type X;n SNe—for example, SN 2014C is an SN Ib;n (Milisavljevic et al. 2015), and PTF11kx is an SN Ia;n. The ";n" label captures the observational properties of the class (the SN-only and interacting phases are independent, observationally) and allows for the application to different SN types. Note that the "n" label indicates narrow emission lines, in accordance with the canonical interaction class (Type IIn), and that in this case "narrow" is relative to SN lines—i.e., the narrow lines are $\lesssim 5000\,km\,s^{-1}$ and not *necessarily* unresolved nor tracing pre-shock CSM.

There are three important reasons to distinguish SNe X;n from promptly interacting SNe that surmount the abhorrence of increasing SN taxonomic entropy. First, that clearly the CSM in an SN X;n is likely molded by different physical processes than that of prompt interactors (PTF11kx is an outlier in the SN Ia-CSM class). Moreover, it is crucial leverage that the underlying SN type in SNe X;n can be unambiguously classified and its explosion energetics inferred from preinteraction spectra and light curves. Finally, distinguishing these events is necessary because studies of SNe X;n require new and unique methods for their discovery, classification, and analysis—for example, the asymptotic hydrodynamic solutions from Chevalier (1982) do not apply to these systems.

Possibly representing SNe Ia;n with the longest delay between explosion and interaction are those SNe Ia with time-variable narrow absorption lines. Such lines in the near-maximum-light spectra heralded interaction for PTF11kx, and individual SNe Ia show evidence for time-variable lines, though much weaker than in the case of PTF11kx (Patat et al. 2007; Simon et al. 2009). In statistical analyses, it has been shown that ∼20% of SNe Ia in S0 or later-type galaxies have time-variable or blueshifted narrow Na I D absorption features (Sternberg et al. 2011, 2014; Maguire et al. 2013). Whether these time-variable and blueshifted absorption features, unaccompanied by later interaction, arise from CSM at $\sim 10^{17}$ cm or unassociated and perhaps more distant interstellar gas is still debated (Chugai 2008; Wang et al. 2008; Borkowski et al. 2009; Bulla et al. 2018), stoked by the fact that these events prefer dusty and gas-rich host galaxies (though the SNe themselves are not necessarily heavily extinguished). If CSM is the origin of these features, interaction would not happen for years and typical SN Ia observations—which only capture the light curve for ∼100 days near-maximum brightness—would not see the interaction.

To measure how frequently 91T-like SNe Ia interact at late times, the *Hubble Space Telescope (HST)* Snapshot survey

GO-14779 (PI M. L. Graham) surveyed 71 SNe with ages of 1–3 yr (nearly all of them SNe Ia, with some SNe IIn) throughout the year 2017 in the near-ultraviolet (NUV). The target list of 80 objects prioritized 91T-like SNe and those with blueshifted Na I D absorption. This program discovered delayed interaction in SN 2015cp (also known as PS15dpq and PTF15fel), confirmed by the presence of broad Hα emission in a follow-up optical spectrum. From the photometric fit, SN 2015cp exploded on 2015 November 1 (approximate day of first light) and thus the NUV detection was on day 681 after explosion. In this paper, all times are reported relative to the day of explosion unless stated otherwise. The only preinteraction optical spectrum available for this event was its classification spectrum 60 days after explosion, which shows no signs of CSM. Details of the full survey and the NUV/optical observations of SN 2015cp are presented by Graham et al. (2018).

In this work, we report radio and X-ray follow-up observations of SN 2015cp and analyze the radio data, using the constant-density shell models of Harris et al. (2016, hereafter "HNK16") to constrain the total mass of CSM and other properties. An overview of the HNK16 models is provided in Section 2. In Section 3, we present the observations of SN 2015cp taken ∼80 days after the NUV detection with the Arcminute Microkelvin Imager (AMI), the Jansky Very Large Array (VLA), and the Neil Gehrels *Swift* Observatory. We analyze the radio nondetections in Section 4 to place upper limits on the CSM mass, extent, and density. In Section 5, we summarize our results, contextualize the constraints with SN Ia progenitor theory, and outline how to systematically find and characterize SNe Ia;n.

2. Interaction Model Summary

HNK16 addressed the scenario of SN Ia ejecta impacting a constant-density, distant, finite-extent shell of CSM. Though we encourage a familiarity with the synchrotron radio light-curve behavior described by HNK16, we will summarize the main conclusions of that work relevant to this study. For more details on these equations, including derivations and normalizations, we refer to HNK16. A glossary of variables is provided in Table 1.

The important hydrodynamic conclusion of the work was a simple equation for the time that the forward shock will reach the outer edge of the CSM shell, which we sometimes refer to as the "end" of interaction. As in HNK16 Equation (5), the inner CSM radius (R_{in}), impact time (t_{imp}), and CSM density (ρ_{csm}) are related through

$$R_{in} \propto t_{imp}^{0.7}\, \rho_{csm}^{-0.1}.$$ (1)

Because the shells have constant density, the mass of a shell is determined by R_{in}, ρ_{csm}, and the CSM fractional width ($f_R \equiv \Delta R / R_{in}$) simply by

$$M_{csm} = \frac{4\pi}{3} \rho_{csm} R_{in}^3 [(1 + f_R)^3 - 1].$$ (2)

Given in HNK16 Equation (7), the time that the forward shock reaches the outer edge of the CSM shell (the time of the radio peak luminosity, t_p) is related to t_{imp} and f_R by

$$t_p \propto t_{imp}\, (1 + f_R)^{1.28}.$$ (3)

Table 1
Glossary of Variables

Symbol	Description	Units in this work	Defining equation
(Preimpact) CSM parameters:			
ρ_{csm}	mass density	g cm^{-3}	
n_{csm}	particle density	cm^{-3}	
m_p	proton mass	g	1.673×10^{-24} g
μ	mean molecular weight		$\rho_{csm} = \mu m_p n_{csm}$
N_{csm}	column density	g cm^{-2}	Equation (5)
R_{in}	inner radius	cm	HNKEq 5
f_R	fractional width		$\Delta R / R_{in}$
M_{csm}	mass	$M_\odot$	Equation (2)
light-curve parameters:			
t_{imp}	time of ejecta impact with CSM	days	
t_p	time of radio peak; time that forward shock overruns CSM	days	HNKEq 7
ν	photon frequency	Hz	
ϵ_B	ratio of magnetic field energy density to gas energy density		
p	power-law slope of relativistic electron density		HNKEq 25
$\mathcal{L}_{\nu,p}$	specific luminosity at radio peak	erg s^{-1} Hz^{-1}	HNKEq 11

Note. HNKEq refers to the equation number in HNK16.

Motivated by nova shells, in HNK16 $f_R = [0.1,1]$, but we ensured through simulation of thicker shells that this relation holds at least up to $f_R = 7$. Using this equation is only appropriate for adiabatic shocks, which we assume is appropriate for our low-density shells; HNK16 Figure 1 shows where cooling is expected to become important. The relation is only weakly dependent on the exact velocity at which the ejecta is truncated, as explored in HNK16 (Figure 7).

The important radiation conclusion was a parameterization for the radio synchrotron light curves. The time that the forward shock reaches the outer edge of the CSM shell is the time of radio peak luminosity. The optically thin peak specific luminosity ($\mathcal{L}_{\nu,p}$, units erg s^{-1} Hz^{-1}) is related to ρ_{csm}, R_{in}, f_R, and frequency (ν) in HNK16 Equation (11),

$$\mathcal{L}_{\nu,p} \propto \nu^{-1} \rho_{csm}^{8/7} R_{in}^{3/7} [1 - (1 + f_R)^{-9/7}], \qquad (4)$$

where the exponent 9/7 is an approximation of the fit value 1.28 to elucidate the relative importance of each factor. As in HNK16, we use $\epsilon_B = 0.1$ as the fraction of energy density in the magnetic field compared to the gas thermal energy density. HNK16 Figure 1 shows which shells are expected to be optically thin at all times. After peak, the radio emission declines rapidly because the CSM shell, heated and accelerated by the shock, quickly rarefies into the near-vacuum that lies outside its outer edge (HNK16 Figure 2). Thus, even a light curve that was not optically thin to synchrotron self-absorption while the shock was inside the shell is likely to become optically thin shortly after peak. HNK16 provides a parameterization for the light-curve decline considering only emission from the shocked CSM (HNK16 Equation (12)), which describes the decline from $\mathcal{L}_p$ to $10^{-3} \mathcal{L}_p$ using only
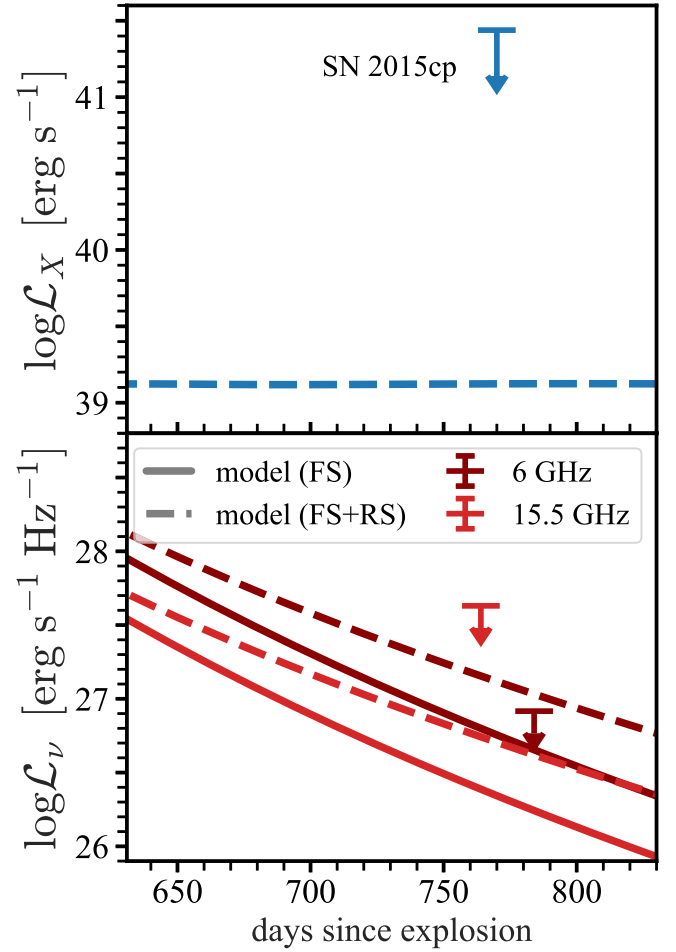

Figure 1. Observations of SN 2015cp (arrows) in X-ray (top panel; 0.5–8 keV *Swift*) and radio (bottom panel; AMI at 15.5 GHz, bright red; VLA at 6 GHz, dark red) compared to a model with $\rho_{csm} = 10^{-19}$ g cm^{-3}, $f_R = 4$, and $t_{imp} = 50$ days created for PTF11kx both including (solid) and excluding (dashed) contribution from the reverse shock.

t_{imp}, f_R, and $\mathcal{L}_{\nu,p}$. We cannot comment on early impacts with thin shells because they would have declined below $10^{-3} \mathcal{L}_{\nu,p}$ by the time of observation and are therefore not captured by this parameterization. A parameterization including the reverse shock emission is given in HNK16 Equation (13). Examples of radio light curves are shown in HNK16 Figures 3 and 4, with Figure 3 showing the light curve including reverse shock emission.

These models were developed with thin nova shells in mind; in such a thin shell, the approximation of constant density is appropriate. How accurately constant-density shell describes a more extended CSM like that of PTF11kx (Silverman et al. 2013b; Graham et al. 2017) is unknown.

3. Observations

Radio and X-ray modeling of the nearest analog to SN 2015cp, PTF11kx, indicated that a PTF11kx-like event at the distance of SN 2015cp (∼170 Mpc) would be visible in the radio and X-rays, though fading (Figure 1). The CSM parameters for these models come from Graham et al. (2017), and the model shown represents the lowest-density possibility for PTF11kx. Synchrotron and bremsstrahlung emission were
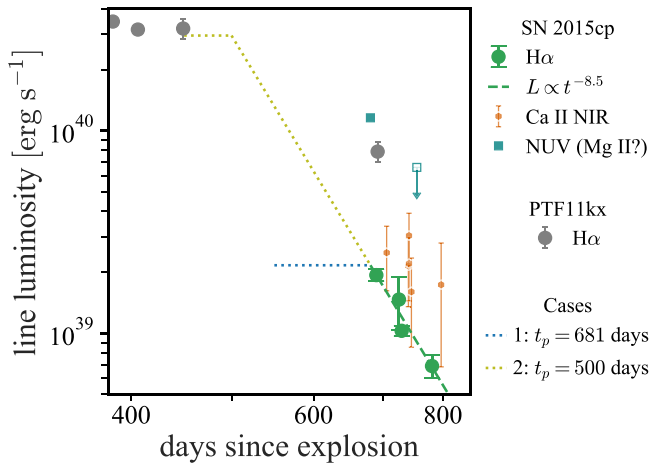
Figure 2. Evolution of the broad Hα emission-line luminosity constrains the duration of interaction for SN 2015cp (green circles), as for PTF11kx (Silverman et al. 2013b, gray circles). The steep decline ($\mathcal{L} \propto t^{-8.5}$; green dashed line) indicates interaction was over by the time of the NUV detection at 681 days. The integrated Ca II near-infrared emission (orange hexagons) and the NUV data that may have been line emission from Mg II (teal squares) are consistent with the Hα decline rate. In this work, we consider two scenarios (dotted): Case 1 (blue), that SN 2015cp is intrinsically fainter than PTF11kx and we discovered SN 2015cp just as interaction ended ($t_p = 681$ days); and Case 2 (yellow), that SN 2015cp had the same Hα luminosity as PTF11kx and its interaction ended at $t_p = 500$ days.
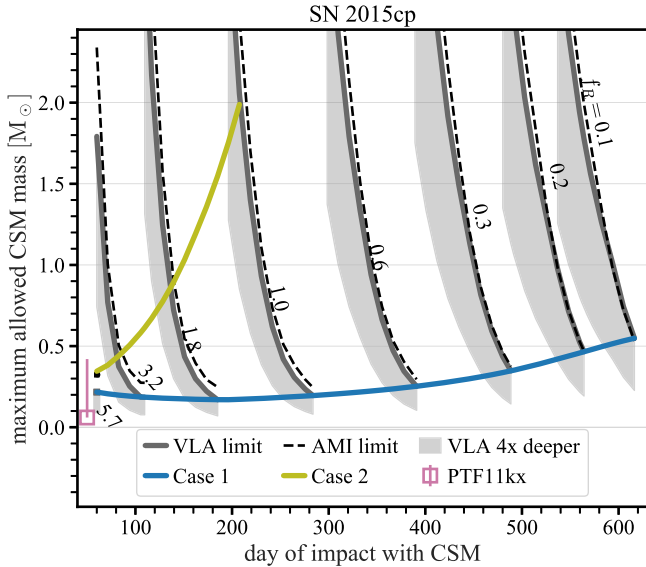
Figure 3. Upper limits on the CSM mass of SN 2015cp as a function of the impact time ($t_{\rm imp}$) and shell width (f_R), assuming a finite-extent, constant-density CSM shell. PTF11kx is shown for comparison (pink open square) for $f_R = 4\text{–}6$ (pink line). Constraints from the 769 days VLA 6 GHz nondetection (gray line) and the 750 days AMI 15.5 GHz nondetection (dashed black line) are similar, highlighting the power of prompt observations. For reference, we illustrate how the constraints would change if the VLA nondetection were four times deeper (gray shading). Cases 1 (blue line) and 2 (yellow line) assume the time of radio peak to 681 and 500 days, respectively, and show the importance of constraining t_p. The CSM mass is constrained to $M_{\rm csm} < 0.5\,M_\odot$ for Case 1 (and $<2\,M_\odot$ for Case 2) despite large uncertainties in the CSM location and extent.

calculated as in that work and HNK16, both including (dashed lines) and excluding (solid lines) emission from the shocked ejecta (Gaunt factors from van Hoof et al. 2014). Unfortunately, no X-ray or radio observations of PTF11kx years after maximum light are known to the authors for a direct
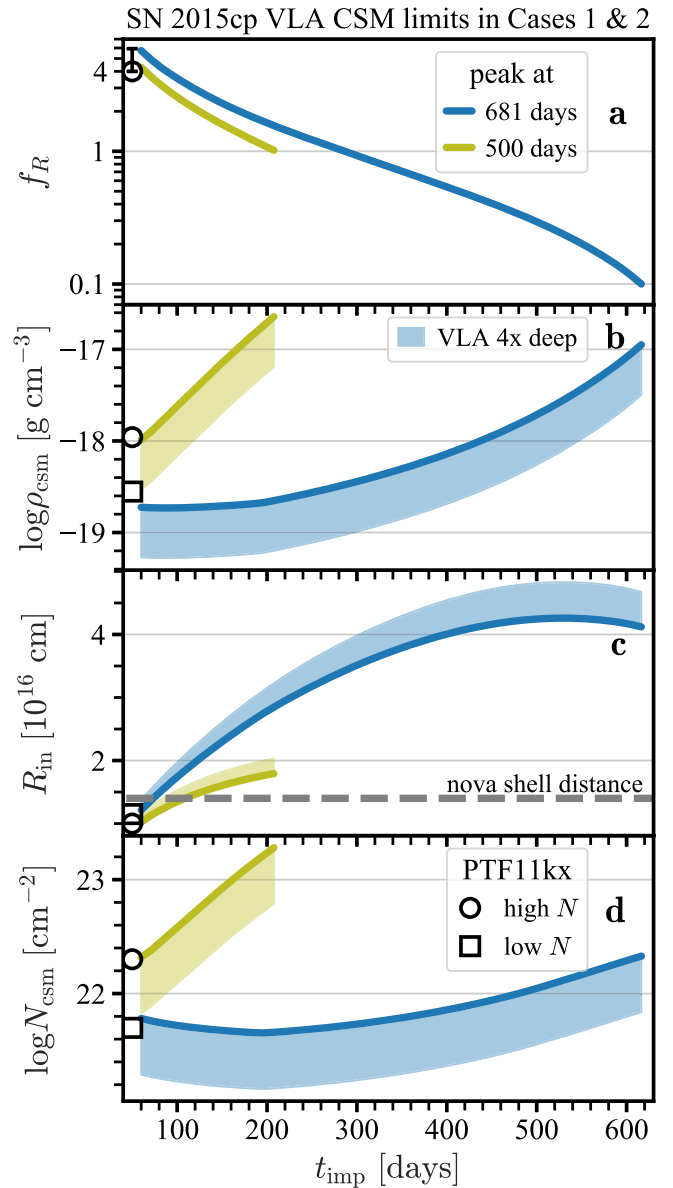

Figure 4. Constraints on CSM properties for Case 1 (blue; radio peak at 681 days) and Case 2 (yellow; peak at 500 days), with a comparison to PTF11kx (open markers). Shaded bands represent the analysis with a nondetection up to four times deeper to illustrate limits. Legends apply to all panels. The panels are (a) fractional width, (b) mass density, (c) inner radius, and (d) column density. Our limits on the inner radius are similar to the expected location of nova shells. Panel (d) shows that a measurement of column density from an optical spectrum near the SN B-band maximum could be leveraged, e.g., 3×10^{22} cm^{-2} would rule out Case 1.

comparison. The light curves demonstrate that AMI and VLA observations had a chance of detecting thick, low-density shells even hundreds of days after interaction has ended. Though not shown here, X-ray observations were promising for denser shells. We therefore pursued observations with the AMI, the Jansky VLA, and the Neil Gehrels *Swift* Observatories, which are summarized in Table 2.

SN 2015cp was observed by the AMI (Zwart et al. 2008; Hickish et al. 2018) on 2017 December 04/19:30:17.7 UT (MJD 58091.82) with a total integration time of 4.96 hr. The AMI-LA is equipped with a digital correlator (Hickish et al. 2018) with a central frequency of 15.5 GHz and a 5 GHz

Table 2
SN 2015cp Radio and X-Ray Observations

UT Date	Instrument	Observed Frequency	3σ limit
2017-12-04	AMI-LA	15.5 GHz	90 μJy
2017-12-24	VLA	6 GHz	17.4 μJy
2017-12-08	Swift-UVOT	4.8 eV	2.3 μJy
2017-12-08	Swift-XRT	1 keV	6.1 nJy

bandwidth spread across 4096 channels. The data were calibrated using the custom reduction pipeline REDUCE_DC (see, e.g., Perrott et al. 2013), which also performs flagging for antenna shadowing, instrumentation errors, and radio frequency interference (RFI). At this stage the data were binned into eight frequency channels and imported into the Common Astronomy Software Applications (CASA) package, where additional RFI flagging and then cleaning were performed to produce an image, which contained a single unresolved source. Fitting this source with the CASA task IMFIT gives its J2000 location as $\alpha = 03^{\mathrm{h}}09^{\mathrm{m}}13\overset{\mathrm{s}}{.}18(2)$, $\delta = +27°34'16\overset{''}{.}8(5)$ with a flux density of 1.24 ± 0.08 mJy. Given that this position is $\sim3'$ from the phase center and the synthesized beam for this observation has major and minor axes of $\sim40''$ and $30''$ (respectively), the object is probably not SN 2015cp. This conclusion is further supported by the position being consistent with a known source in the NVSS archive (Condon et al. 1998). The root mean square (rms) at the phase center of the AMI-LA image is $\sim30\ \mu$Jy, so we set a 3σ upper limit on the 15.5 GHz radio emission from SN 2015cp of $\sim90\ \mu$Jy.

On UT 2017 December 24, we observed SN 2015cp with the VLA (under program 17B-434, PI Horesh) at a central frequency of 6 GHz (C-band) and undertaken in the B configuration. We used J0329+2756 and 3C 138 for phase and flux calibration, respectively, and reduced the data using standard CASA calibration and imaging routines. The observation resulted in a null detection with a 5.8 μJy rms, corresponding to a 3σ upper limit of 17.4 μJy.

From UT 2017 December 8 through 2017 December 9, we observed SN 2015cp with the UVOT and XRT instruments on *Swift*. No source is detected in a 4.9 ks UVOT exposure using the UVW1 filter, nor are any counts detected near the source position in the 6.1 ks (livetime, 0.5–8 keV) XRT exposure. Using the *Swift*-UVOT zeropoints,[14] we derive a 3σ limiting magnitude of 23 in the AB system. Assuming only absorption by the Galaxy in the direction of the SN (with $N_{\mathrm{H}} = 1.1 \times 10^{21}\ \mathrm{cm}^{-2}$; Kalberla et al. 2005) and assuming a spectrum with photon index $\Gamma = 2$, we derive a 3σ limiting X-ray flux of $4.1 \times 10^{-14}\ \mathrm{erg\ cm}^{-2}\,\mathrm{s}^{-1}$ (0.5–8 keV).

4. Limits on the CSM of SN 2015cp

In this section, we use the constant-density, finite-extent CSM radio light-curve models of HNK16 to limit the CSM properties given our radio nondetections. The direct observational considerations in this analysis are that (1) impact occurred at >60 days, (2) our earliest radio limit is at 764 days, and (3) our deepest radio limit is at 784 days. In Section 4.1, we will consider the NUV and optical observations to argue that the bulk of the CSM had been swept over by the time of the NUV observation, and define two scenarios that we consider likely for the time of radio peak (Cases 1 and 2). In Section 4.2, we

translate the radio upper limits into CSM mass limits, from which we see the importance of regular monitoring of interaction candidates and of rapid radio follow-up observations. Finally, we investigate other properties of the maximum-mass CSM shells allowed by our radio nondetections and show that their column densities are high enough that preimpact spectra could show narrow absorption features as in PTF11kx; this, combined with the lack of absorption features in the preimpact spectrum, indicates that the CSM is probably low density as assumed.

4.1. Constraining the Duration of Interaction

In Section 4.2, we will see that constraining the time at which interaction ends (t_p; the time the forward shock reaches the edge of the shell) or the time of impact (t_{imp}) increases the utility of the radio data. To the purpose of constraining the interaction timescale, we compare SN 2015cp to its nearest analog, PTF11kx, using the metric that indicated the interaction history of that object: the integrated luminosity of the broad Hα line ($\mathcal{L}_{\mathrm{H}\alpha}$) from Silverman et al. (2013b).

In Figure 2, we show $\mathcal{L}_{\mathrm{H}\alpha}$ for PTF11kx and SN 2015cp. Note that the point with large error bars is a combination of three measurements, with uncertainties reflecting systematic and statistical errors. For SN 2015cp we also include the line luminosity of the Ca II near-infrared triplet and the NUV observations presented and discussed by Graham et al. (2018) which may be an Mg II line. The Ca II and NUV signals have decline rates consistent with that of $\mathcal{L}_{\mathrm{H}\alpha}$. No SN Ia features are seen in the spectrum; all of these lines are powered by interaction.

As seen in Figure 2, PTF11kx and SN 2015cp have very different spectroscopic coverage: the former has observations throughout the years, whereas the latter sampling is of the decline only but at comparatively high cadence. For PTF11kx, we know $\mathcal{L}_{\mathrm{H}\alpha}$ increased until 285 days, plateaued for the next 160 days, and started to decline sometime between 450 and 695 days. The decline was interpreted as the time at which the shock had swept over the majority of the CSM such that the reservoir of shocked, cooling gas was depleted (Silverman et al. 2013a), constraining $450 \leqslant t_p \leqslant 690$ days, yet leaving the $\mathcal{L}_{\mathrm{H}\alpha}$ decline rate highly uncertain. (We note that this interpretation is not based on detailed hydrodynamic and radiation transport calculations, so there is an additional but currently unquantified level of uncertainty in this interpretation that requires sophisticated modeling to understand, which is far beyond the scope of this work.) In contrast, SN 2015cp has no spectra between its classification spectrum (~60 days) and the X-Shooter spectrum (706 days), so its impact time and peak time are poorly constrained. But its decline is well observed by the follow-up campaign. Over the observed 100 days, SN 2015cp has $\mathcal{L}_{\mathrm{H}\alpha} \propto t^{-8.5}$ (from an error-weighted fit to the data performed with scipy).

The fortuitous observations of both SNe with optical spectra at ~60 and 700 days allows us at least to say that these SNe are not twins. SN 2015cp is an order of magnitude fainter in Hα at late times, and began interacting with its CSM later—the classification spectrum was of sufficient quality to detect, at 3σ confidence, a narrow Hα line an order of magnitude less luminous than was observed in PTF11kx (Graham et al. 2018)

If we knew the peak Hα luminosity reached by SN 2015cp, we would be able to constrain the time interaction ended. Since we do not have these data, we consider two cases representing different conservative assumptions, illustrated in Figure 2.

---

[14] https://swift.gsfc.nasa.gov/analysis/uvot_digest/zeropts.html

1. Case 1 assumes SN 2015cp was brightest in Hα at NUV discovery, i.e., $t_p = 681$ days. This would not be as serendipitous as it may, at first, seem: detection favors the bright, and the Hα luminosity was likely highest just before interaction ended—when the reservoir of cooling shocked hydrogen is greatest.

2. Case 2 assumes the observed $\mathcal{L}_{H\alpha}$ decline rate is constant *and* that SN 2015cp had the same maximum $\mathcal{L}_{H\alpha}$ as PTF11kx, resulting in $t_p = 500$ days. Furthermore, if PTF11kx and SN 2015cp had the same CSM density, then, like PTF11kx, SN 2015cp would have needed 282 days to reach the plateau luminosity, so for this case $t_{imp} \leqslant 218$ days. Furthermore, this comparison implies that for PTF11kx $t_{p,11kx} = 588$ days (if it follows the same decline rate) so $f_{R,11kx} = 5.9$.

Case 1 is our favored scenario because it has fewer assumptions: Case 2 relies on both extrapolation and a comparison to PTF11kx that may not be appropriate.

Finally, we note that the limits obtained in Cases 1 and 2 bound what would be obtained from assuming the $t^{8.5}$ decline rate and any $500 \leqslant t_p \leqslant 681$.

4.2. Mass Limits from Radio Data

Using these parameterized light curves described in Section 2, we can determine the maximum CSM mass allowed by our VLA and AMI nondetections, with particular consideration given to the two cases put forth in the previous section.

The methodology is straightforward. We create a grid of models varying t_{imp} and f_R such that there are a variety of peak times (i.e., a variety of delay times between radio peak and AMI/VLA observation). For each model light curve we know the maximum $\mathcal{L}_p$ allowed by the AMI/VLA limit, which translates into a maximum allowed density. From t_{imp}, f_R, and the maximum allowed density we then know the maximum allowed mass (see Equations (1) and (2)).

From observations, $t_{imp} \geqslant 60$ days and $t_p \leqslant 681$ days. In line with HNK16, we only consider $f_R \geqslant 0.1$. These criteria set our explored parameter space to $t_{imp} \in [60, 616]$ days and $f_R \in [0.1, 5.74]$. Cases 1 and 2 fix t_p to a particular value and represent a specific contour in t_{imp}–f_R space (and in Case 2, $t_{imp} \leqslant 208$ days, i.e., $f_R \geqslant 1.02$; Equation (3)).

The mass limits resulting from this analysis are shown in Figure 3. It is important to acknowledge that the mass constraints from the VLA data and the AMI data are nearly the same, highlighting the power of rapid follow-up observations for these steeply declining light curves. The VLA limit is 11 times deeper than that of AMI, after accounting for the spectral energy distribution and the observed frequency, but the AMI limit is as effective simply by virtue of occurring three weeks earlier. For reference, we also present how the maximum allowed mass would decrease if the VLA nondetection were four times deeper, to simulate a longer exposure time or a closer object and to indicate that these are upper limits.

Given an f_R, there is a maximum possible impact time that satisfies the requirement $t_p < 681$ days, setting the latest t_{imp} for each f_R curve. The thickest possible shell has only one valid impact time, while thinner shells span more of the domain. For curves thinner than $f_R \approx 1$, the shaded regions also appear to have an earliest possible impact time, but this is simply due to the limitations of the parameterized light curves (Section 2).

The steep slope of each f_R curve reflects the steep decline of the light curves.

The degeneracy between f_R and t_{imp}, as well as the sensitive dependence of the mass limit on t_{imp}, are obvious in this plot and motivated the search for additional constraints on the duration of interaction described in Section 4.1. We consider two cases: Case 1, the radio light curves peak at $t_p = 681$ days; and Case 2, $t_p = 500$ days. A fixed t_p gives a relation between f_R and t_{imp} rather than a constraint on either parameter alone (Equation (3)) as demonstrated by the curves in Figure 3. In fact, t_p constrains the CSM mass very well almost independent of the inaccuracy in t_{imp} and f_R. For this reason, we identify it as the key parameter to constrain in future efforts to characterize SNe Ia;n.

The VLA nondetection constrains the CSM mass to $M_{csm} < 0.5\,M_\odot$ for Case 1 and $M_{csm} < 2\,M_\odot$ for Case 2. Particularly in Case 1, these limits are similar to the mass measured for PTF11kx (Graham et al. 2017), as shown. We show both the reported $M_{csm,11kx} = 0.06\,M_\odot$ as well as a higher estimate of $M_{csm,11kx} = 0.42\,M_\odot$ that results from assuming the four-times-higher column density reported by the authors as well as the result from this work that the CSM may have been thicker than previously assumed (Section 4.1).

4.3. The Constraining Power of Preimpact Spectra

In this section, we translate the VLA upper limit into limits on the CSM column density (N_{csm}) and its constituent factors: f_R, R_{in}, and ρ_{csm}. For PTF11kx, the saturated narrow absorption lines in the preimpact optical spectra alerted observers to the unique nature of the event. Borkowski et al. (2009) identify the narrow Na D features as a good metric for CSM shell properties when considering shells at $>10^{17}$ cm, and we expect the same is true for nearer cases. This analysis is relevant for future observations rather than SN 2015cp itself, whose only preimpact spectrum is too late to have revealed such features. The measurements for PTF11kx referenced in this analysis come from Graham et al. (2017).

The constituents of the column density are f_R, R_{in}, and ρ_{csm}:

$$N_{csm} = n_{csm} f_R R_{in} = \rho_{csm} f_R R_{in}/(\mu m_p). \qquad (5)$$

For this analysis, we have assumed the mean molecular weight $\mu = 1.33$. In the above equation, n_{csm} is the particle density and m_p is the proton mass.

In Figure 4, we show these constraints for Cases 1 and 2 again as a function of t_{imp}. As in Figure 3, shaded bands represent a simulated VLA nondetection up to four times deeper than the actual nondetection. We also show the value of each parameter for PTF11kx as derived by Graham et al. (2017), noting both the higher and lower reported values for the column density. The equations provided in Section 2 are a helpful reference when interpreting the behavior of the curves in panels (a)–(c).

Panel (a) simply illustrates the relationship between f_R and t_{imp} for a fixed t_p and is independent of the VLA limit. Earlier t_{imp} values require wider shells to peak at a given time. The error bar on the PTF11kx point indicates the fractional width $f_{R,11kx} = 5.9$ that would be implied if interaction ended at 588 days (Section 4.1).

Panel (b) shows upper limits on CSM density. The Case 2 limit is higher (weaker) than the Case 1 limit because the light curve has had more time to decline, so higher peak luminosities and thus higher densities are permissible. Later impact times

also allow higher ρ_{csm} (for a given t_p) because thinner shells have a lower peak luminosity and faster decline rate than thicker shells. For PTF11kx, this value is derived using measurements of f_R, t_{imp}, and N_{csm}.

In panel *(c)*, we plot the limit on R_{in}, which is actually a lower limit. While generally the behavior of this curve is intuitive (one would expect a later impact time to imply a more distant shell), the weak dependence of R_{in} on ρ_{csm} actually requires that higher-density shells be nearer to the SN for interaction to begin at a given time, resulting in a maximum R_{in}. The dependence on ρ_{csm} is also why a deeper VLA limit (shaded band), constraining the CSM to lower densities, would imply a higher R_{in}. The value for PTF11kx comes from t_{imp} and assuming a maximum ejecta speed, but is consistent with the HNK16 value given its t_{imp} and ρ_{csm}.

Finally, in panel *(d)*, we use Equation (5) to translate our radio nondetections into an upper limit on N_{csm}. As with the mass constraint previously, fixing t_p results in limits on N_{csm} that are almost independent of t_{imp}, particularly for Case 1.

While N_{csm} is not single-valued, we see that a reliable measurement of N_{csm} from a spectrum near-maximum B-band brightness could constrain t_p by making Case 1 (i.e., late values of t_p) less likely. The Ca K absorption line in PTF11kx that was used to measure N_{csm} was strong up to at least 20 days after maximum light, so this metric does not necessarily require very early-time spectra (but does benefit from high-resolution spectra).

5. Conclusions and Discussion

SN 2015cp is the third case of an SN Ia interacting with CSM located $\sim 10^{16}$ cm from the progenitor system, what we call an SN Ia;n. The "X;n" label designates a supernova that initially appears normal, but weeks to months after SN peak is dominated by interaction signatures. Here we will summarize our radio and X-ray nondetections and the constraints on the circumstellar environment of SN 2015cp obtained via the models of (Harris et al. 2016, "HNK16"). We will then put these limits in context of SN Ia progenitor theory and other known interacting SNe Ia. Finally, we will highlight the need for a systematic search for SNe Ia;n and make suggestions based on the lessons learned from our analysis of both PTF11kx and SN 2015cp.

This work relies on the hydrodynamic modeling and radiation calculations of HNK16, which we summarized briefly in Section 2. These models address the scenario of an adiabatic shock propagating through a constant-density CSM shell with a distinct inner and outer edge. When the forward shock reaches the edge of the CSM, we say interaction has "ended" because the CSM is no longer gaining thermal energy; this is the time of peak radio luminosity. In HNK16, a simple description of the relevant hydrodynamic timescales and the optically thin radio synchrotron light curves was derived.

As described in Section 3 and shown in Figure 1, at a distance of 167 Mpc, SN 2015cp was a good candidate for radio and X-ray follow-up observations once interaction was discovered. Models of its nearest analog, PTF11kx, suggested SN 2015cp could still be visible even if (like PTF11kx) interaction had ceased—that interaction had ended for SN 2015cp was unknown at the time of the observations. Therefore, we observed this target with the VLA, AMI, and *Swift*; but all observations resulted in nondetections.
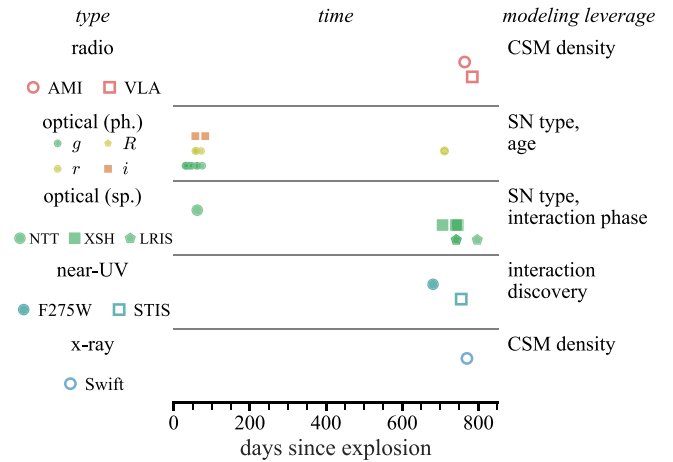

Figure 5. Summary of the panchromatic data available for SN 2015cp and how they are used in our analysis. Optical observations are split by whether they are photometric imaging ("ph.") or spectroscopy ("sp."). Legends indicate the instrument or filter used, and nondetections are open markers. The two-year gap between the initial discovery and classification of this supernova and the discovery of its interaction creates large uncertainties in its CSM properties.

Nevertheless, the radio upper limits can be interpreted in the framework of Harris et al. (2016) to give limits on the CSM properties. The extent of the CSM is a key parameter in these models, and can be determined if the time of impact and time that the forward shock sweeps over the bulk of the CSM are known. In the case of SN 2015cp, we can only place limits on these times (Section 4.1). For both SN 2015cp and PTF11kx, the limits on the duration of interaction come from the evolution of the Hα luminosity. The decline of both the optical and NUV emission suggests that the shock was no longer energizing CSM by the time of our observations. We assess two scenarios, which can be thought of as late and early limits on the time interaction ended: Case 1, in which the radio light curve peaked at the time of NUV discovery (681 days); and Case 2, in which the radio light curve peaked at 500 days, under the assumption that the Hα luminosity of SN 2015cp was the same as that of PTF11kx and a constant decline rate (Figure 2). Without these assumptions there is too large an uncertainty in t_{imp}–f_R space to draw conclusions (Figure 3).

In Section 4.2, we find that the CSM has a mass $M_{csm} < 0.5\, M_\odot$ for Case 1. Case 2 is less constraining because it implies our observations occur longer after peak radio brightness than in Case 1; in Case 2, $M_{csm} < 2\, M_\odot$ (Figure 3). These limits are near to the inferred CSM mass of PTF11kx, but far higher than the estimated mass from a single nova shell eruption, which for the symbiotic recurrent nova RS Ophiuchi was observed to be $\sim 10^{-6}\, M_\odot$ (O'Brien et al. 1992).

We also explored the limits on CSM extent, density, inner radius, and column density that can be derived from the radio observations (Section 4.3; Figure 4). We find that in Case 1 the CSM of SN 2015cp had, at most, the same column density as PTF11kx. For Case 2, higher column densities are allowed. The lack of any narrow absorption features in the preimpact spectrum supports the idea that SN 2015cp had a lower column density than PTF11kx, which in turn implies a lower density ($\sim 10^{-19}$ g cm^{-3}), though it may be the case that the spectrum was too late to see the feature.

Figure 5 summarizes how the various observations of SN 2015cp have been employed to constrain the CSM properties.

As with promptly interacting SNe Ia, SNe Ia;n are associated with the "91T-like" subclass. Here we define this as spectroscopically most similar to SN 1991T or SN 1999aa near-maximum light, with the light-curve similarities being a secondary classification metric when a near-maximum spectrum is lacking. The physical connection between these three groups is undetermined. The simplest hypothesis to explain the similarity of the spectroscopic SN features is that the groups share the same progenitor system. But, particularly for the prompt interaction cases, which lack a noninteracting phase for studying the SN alone, some debate whether the progenitor is a high mass star (e.g., Inserra et al. 2016). Silverman et al. (2013a) also noted that PTF11kx differed from promptly interacting SNe Ia-CSM. Further studies, both observational and theoretical of SNe Ia;n, are needed to establish the connection between 91T-like SNe Ia, SNe Ia;n, and promptly interacting SNe Ia-CSM for certain.

If the systems do have a common progenitor, eruptive mass-loss episodes could naturally bridge noninteracting, late-interacting, and promptly interacting SNe Ia. An eruptive mass-loss episode can quickly (within years) sweep extended CSM into a shell at a distance of $\sim 10^{16}$ cm (Moore & Bildsten 2012), which would then mix with the interstellar medium within $\sim 10^6$ years. This would explain why some 91T-like SNe Ia have clean environments (like SN 1991T) while others interact with CSM at $\sim 10^{16}$–10^{17} cm. Furthermore, multiple eruptions will result in CSM shells collected near the same radius such that the CSM mass observed in the interaction need not represent that of a single eruption (and swept up material). Prompt interaction would be observed if the SN occurred while extended material was still in the progenitor system, i.e., before an eruption. Thus, the three observed groups are natural in an eruptive-mass-loss scenario.

However, even determining that eruptions form the CSM does not by itself reveal the nature of the progenitor system, as there are a variety of mechanisms for rapid mass loss that evacuate an inner cavity. Novae and symbiotic novae are the canonical example, and are tied to the SD progenitor channel. The DD scenario of Shen et al. (2013) also has a rapid expulsion of mass in a common envelope phase, though without a sufficient density, and is too distant to explain observed SNe Ia;n. It has also been suggested that a CO WD merging with the core of a post-AGB star can create a variety of interaction timescales (e.g., Soker 2013). In the core-collapse hypothesis, the ejections that create the CSM may be caused by instabilities within the star or a binary companion; but whether this is relevant for SNe Ia;n is unclear, as Inserra et al. (2016) found that PTF11kx was the only SN Ia-CSM for which they would not favor a core-collapse progenitor. Characterizing the mass, location, and extent of the CSM in SNe Ia;n can distinguish these scenarios from one another.

Determining the origin of the CSM in SNe Ia;n and possibly thus the progenitors of 91T-like SNe Ia relies partially on increasing our sample of SNe Ia;n with a systematic observation strategy. From our analyses of PTF11kx, and now SN 2015cp, some guidelines for future efforts to discover and characterize SNe Ia;n emerge. The first suggestion is to ensure that nearby 91T-like SNe Ia are monitored over a years-long baseline, to discover the onset of interaction: our analysis shows that the two-year gap in observations of SN 2015cp severely limits our ability to use the radio nondetections a priori. Long-term photometric monitoring is possible with the Zwicky Transient Facility (and, in the future, the Large Synoptic Survey Telescope) and discovery should be possible with such surveys because Hα holds the R-band magnitude constant months after SN peak (Wood-Vasey et al. 2004; Dilday et al. 2012). Obtaining spectroscopic confirmation of the SN subtype is also important and should be feasible if not rote for targets that are within 200 Mpc (which are the best-suited targets for radio and X-ray follow-up). After discovery of interaction, regular spectroscopy or imaging with a narrow Hα filter to measure the Hα line strength is strongly encouraged, as it is a proxy for the phase of interaction. We have shown that radio observations should prioritize being early over being deep: the AMI nondetection was nearly as constraining as that of the VLA. In the case of a radio detection, of course, the capability of the VLA to provide a spectrum would be crucial and a time series useful. X-ray observations also constrain the CSM mass and are likely from thermal bremsstrahlung, thus independent of the synchrotron ϵ_B parameter. If the Hα emission is observed to be constant or increasing, a radio or X-ray nondetection may indicate a high optical depth in which case continued monitoring (or a different frequency observation) would be prudent. Therefore, we suggest that continual monitoring of 91T-like SNe Ia with a plan for rapid combined radio and optical follow-up observations is the path forward for growing our sample of SNe Ia;n and understanding the progenitors of 91T-like SNe Ia.

ORCID iDs

P. E. Nugent ⓘ https://orcid.org/0000-0002-3389-0586
M. L. Graham ⓘ https://orcid.org/0000-0002-9154-3136
M. Smith ⓘ https://orcid.org/0000-0002-3321-1432
N. Butler ⓘ https://orcid.org/0000-0002-9110-6673
S. Valenti ⓘ https://orcid.org/0000-0001-8818-0795
A. V. Filippenko ⓘ https://orcid.org/0000-0003-3460-0103
O. Fox ⓘ https://orcid.org/0000-0003-2238-1572
P. L. Kelly ⓘ https://orcid.org/0000-0003-3142-997X
K. J. Shen ⓘ https://orcid.org/0000-0002-9632-6106

References

Borkowski, K. J., Blondin, J. M., & Reynolds, S. P. 2009, ApJL, 699, L64
Branch, D., Fisher, A., & Nugent, P. 1993, AJ, 106, 2383
Branch, D., Livio, M., Yungelson, L. R., Boffi, F. R., & Baron, E. 1995, PASP, 107, 1019
Bulla, M., Goobar, A., & Dhawan, S. 2018, MNRAS, 479, 3663
Chevalier, R. A. 1982, ApJ, 258, 790
Chomiuk, L., Soderberg, A. M., Chevalier, R. A., et al. 2016, ApJ, 821, 119
Chugai, N. N. 2008, AstL, 34, 389
Condon, J. J., Cotton, W. D., Greisen, E. W., et al. 1998, AJ, 115, 1693
Dilday, B., Howell, D. A., Cenko, S. B., et al. 2012, Sci, 337, 942
Filippenko, A. V. 1997, ARA&A, 35, 309
Filippenko, A. V., Richmond, M. W., Matheson, T., et al. 1992, ApJL, 384, L15
Fink, M., Röpke, F. K., Hillebrandt, W., et al. 2010, A&A, 514, A53
Fransson, C., Larsson, J., Migotto, K., et al. 2015, ApJL, 806, L19
Garavini, G., Folatelli, G., Goobar, A., et al. 2004, AJ, 128, 387
Graham, M. L., Harris, C. E., Fox, O. D., et al. 2017, ApJ, 843, 102
Graham, M. L., Harris, C. E., Nugent, P. E., et al. 2018, ApJ, submitted
Harris, C. E., Nugent, P. E., & Kasen, D. N. 2016, ApJ, 823, 100
Hickish, J., Razavi-Ghods, N., Perrott, Y. C., et al. 2018, MNRAS, 475, 5677
Hunter, J. D. 2007, CSE, 9, 90
Inserra, C., Fraser, M., Smartt, S. J., et al. 2016, MNRAS, 459, 2721
Jones, E., Oliphant, T., Peterson, P., et al. 2001, SciPy: Open Source Scientific Tools for Python, http://www.scipy.org/
Kalberla, P. M. W., Burton, W. B., Hartmann, D., et al. 2005, A&A, 440, 775
Larsson, J., Fransson, C., Östlin, G., et al. 2011, Natur, 474, 484
Leloudas, G., Hsiao, E. Y., Johansson, J., et al. 2015, A&A, 574, A61
Maguire, K., Sullivan, M., Patat, F., et al. 2013, MNRAS, 436, 222
Mauerhan, J. C., Filippenko, A. V., Zheng, W., et al. 2018, MNRAS, 478, 5050
McMullin, J. P., Waters, B., Schiebel, D., Young, W., & Golap, K. 2007, in ASP Conf. Ser. 376, Astronomical Data Analysis Software and Systems XVI, ed. R. A. Shaw, F. Hill, & D. J. Bell (San Francisco, CA: ASP), 127
Milisavljevic, D., Margutti, R., Kamble, A., et al. 2015, ApJ, 815, 120
Moore, K., & Bildsten, L. 2012, ApJ, 761, 182
O'Brien, T. J., Bode, M. F., & Kahn, F. D. 1992, MNRAS, 255, 683
Oliphant, T. 2006, A Guide to NumPy (Spanish Fork, UT: Trelgol)
Patat, F., Chandra, P., Chevalier, R., et al. 2007, Sci, 317, 924
Perrott, Y. C., Scaife, A. M. M., Green, D. A., et al. 2013, MNRAS, 429, 3330
Raskin, C., & Kasen, D. 2013, ApJ, 772, 1
Astropy Collaboration, Robitaille, T. P., Tollerud, E. J., et al. 2013, A&A, 558, A33
Shen, K. J., Guillochon, J., & Foley, R. J. 2013, ApJL, 770, L35
Shen, K. J., & Moore, K. 2014, ApJ, 797, 46
Silverman, J. M., Nugent, P. E., Gal-Yam, A., et al. 2013a, ApJS, 207, 3
Silverman, J. M., Nugent, P. E., Gal-Yam, A., et al. 2013b, ApJ, 772, 125
Simon, J. D., Gal-Yam, A., Gnat, O., et al. 2009, ApJ, 702, 1157
Soker, N. 2013, in IAU Symp.281, Binary Paths to Type Ia Supernovae Explosions, ed. R. Di Stefano, M. Orio, & M. Moe (Cambridge Univ. Press: Cambridge), 72
Sternberg, A., Gal-Yam, A., Simon, J. D., et al. 2011, Sci, 333, 856
Sternberg, A., Gal-Yam, A., Simon, J. D., et al. 2014, MNRAS, 443, 1849
van Hoof, P. A. M., Williams, R. J. R., Volk, K., et al. 2014, MNRAS, 444, 420
Wang, X., Li, W., Filippenko, A. V., et al. 2008, ApJ, 675, 626
Wood-Vasey, W. M., Wang, L., & Aldering, G. 2004, ApJ, 616, 339
Zwart, J. T. L., Barker, R. W., Biddulph, P., et al. 2008, MNRAS, 391, 1545